Basics of Molecular Beam Epitaxy (MBE) technique

Book · January 2013

CITATIONS
0

READS
9,980

1 author:

Lorenzo Morresi
University of Camerino
27 PUBLICATIONS **438** CITATIONS

SEE PROFILE

Send Orders of Reprints at reprints@benthamscience.net
Silicon Based Thin Film Solar Cells, 2013, 81-107

CHAPTER 4

Molecular Beam Epitaxy (MBE)

Lorenzo Morresi*

University of Camerino-School of Science and Technology-Physics Division, Via Madonna delle Carceri, 9-62032 CAMERINO (MC), Italy

Abstract: Molecular Beam Epitaxy (MBE) represents a widely used growth technique to approach the basic research applied to the growth of semiconductor films and multilayer structures. The main features that distinguish the MBE from other growth techniques are the precise reproducibility of all parameters involved during the epitaxial process, the growth conditions far from thermodynamic equilibrium, and the possibility of controling the kinetic evolution of the outermost layers of the epitaxial film. Nowadays, MBE is also used to grow and investigate nanosized semiconducting materials, which are profoundly interesting for photovoltaic future applications as well.

Keywords: Molecular beam epitaxy, semiconductor thin films, nucleation in film growth, nanocrystalline materials, electron beam deposition, doping thin films, impurities in crystals, quantum dots, RHEED, surface reconstruction, dislocations.

1. INTRODUCTION

Molecular Beam Epitaxy (MBE) is a technology used for the deposition of thin film compound semiconductors, metals or insulators that allows a precise control of compositional profiles by using a process far from the thermodynamic equilibrium. The term epitaxy originates from the Greek roots “epi” and “taxis” which mean to arrange upon. In other words, the epitaxy is the arrangement of one or more thermal particles atop a heated and ordered crystalline substrate to form a thin layer whose crystallinity matches that of the substrate even though the composition of the materials may differ (*e.g.* SiGe/Si, GaAlAs/GaAs, CdTe/GaAs,…). Again, the term beam means that evaporated elements (atoms and/or molecules) do not interact with each other or with vacuum chamber gases until they impinge the substrate because of their long mean free paths which are involved in the deposition process.

This unique growth technique is widely used to produce superlattice structures consisting of many alternate thin layers with single thickness as low as ~10 Å. Furthermore, impurities are evaporated onto the growing film through separate sources. In this way the doping profile, orthogonal to the surface, may be varied and controlled with a spatial resolution not easily achieved by more conventional techniques.

MBE was developed by Alfred Cho and John Arthur at Bell Telephone Labs in the early 1970s, in

***Address correspondence to Lorenzo Morresi:** University of Camerino, School of Science and Technology, Physics Division, Via Madonna delle Carceri 9, Camerino, 62032, Italy; Tel: +39 333 9961198/+39 737 402528; Fax: +39 737402853; E-mail: lorenzo.morresi@unicam.it

an attempt to develop a new variety of high-frequency and high-temperature devices such as injection lasers, electro-optic phase modulators, photocathodes and oscillators [1], as well as IMPATT diodes [2], mixer diodes [3] and optical waveguides [4] all based on the same requirement: the development of thin layer structures. Their pioneering work was focused mainly on preparing $A_{III}B_V$ compound films (like GaAs) overlapping compliance due to the large difference in vapor pressures between the group III and group V elements. Their efforts bring to the formation of stoichiometric III-V films by the molecular beam epitaxy method, and demonstrated by optical and electron diffraction measurements [5, 6].

Adding the Auger spectroscopy for the surface chemical analysis to the vacuum system, and the reflection electron diffraction for *in situ* structural analysis, they were able to resolve the original uncertainties over film stoichiometry and substrate cleanliness. Improving the characterization of both the epitaxial layer and the substrate by incorporating these surface diagnostic techniques into the chamber process, the progress in MBE was very rapid.

The strength of this particular growth process is due to the very low deposition rates (generally few Å per second) generated by the sublimation of extremely pure solid elements heated in separate effusion cells (mostly based on Knudsen concept). In fact, the source material is transformed into its gaseous state by raising its vapor pressure through an increase in temperature. The gaseous particles expand into the evacuated space between the orifice's source and the substrate, where the condensation process takes place. The condensate reacts with the surface until the epitaxial arrangement takes place and the crystalline structure grows with a comparable growth rate. To reduce the impurity levels in the growing layers to an as low as possible value, the epitaxial growth occurs in Ultra-High-Vacuum (UHV) conditions, with a total pressure within the deposition chamber lower than 10^{-10} Torr.

Intricate structures of few monolayers (MLs) composed by different materials may be fabricated by controling the movements of shutters placed in front of each evaporator source. Such control has allowed the development of structures with abrupt and sharp interfaces where the charge carriers can be bi-dimensionally confined in space, due to quantum wells [7-10], or even one-dimensionally confined, due to quantum dots [11-13]. Such layers are nowadays a critical part of many modern semiconductor devices (Fig. **1**), including semiconductor lasers [14-16], light-emitting diodes [17], photodetectors [18, 19] and solar cells [20-23].

The UHV conditions in the environment and control of the quality of the source materials allow much higher film purity, compared to other growth techniques.

Moreover, the vacuum condition allows for the use of electron diffraction probes, which provide fundamental information on the growth mechanisms. On the other hand, MBE suffers of lower yield compared to other techniques such as Liquid Phase Epitaxy (LPE), Metal-Organic Vapor Phase Deposition (MOCVD), Sputtering and Plasma Enhanced Chemical Vapor Deposition (PECVD) due to a lower speed process and dimension wafer capability.

2. MBE SYSTEM

A molecular beam epitaxy system is basically a vacuum evaporation apparatus. What may be considered a standard MBE system is shown schematically in Fig. **2**.

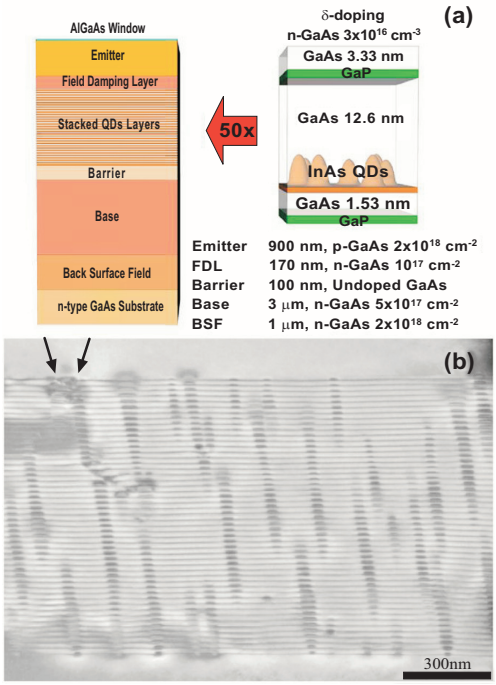

Figure 1: (a) Structure of the 50 stacked quantum dot solar cell grown by MBE. Each GaP layer has a nominal thickness of 1 ML = 0.273 nm. (b) Cross-sectional TEM image of the 50 stacked quantum dot layers. The arrows indicate the defects observable in the image (AIP license n. 2546451267415).

The system consists of a stainless-steel growth chamber connected to other chambers by gate valves. These latter are needed to avoid contamination of components and materials sources by both external and process gases, and to maintain pressure into the growth chamber as low as possible. Modern systems are provided with a proper treatment chamber, and a load lock module represents the only way to transfer the sample to and from the air.

The pumping system, a combination of ion pump, titanium sublimation pump and liquid N_2 cryopanels, can reduce the residual impurity density to a minimum. The two parameters that characterize the vacuum into the growth chamber are: the mean free path, L, (average distance traversed by reactant gas molecules between successive collisions), and the partial pressure of the residual gas molecules, p_r. The highest admissible p_r value depends on L being larger than the distance from the outlet orifice of the beam source to the substrate surface ($L > 0.2$ m).

Using the ordinary assumptions of the kinetic theory of an ideal gas and, for example, the typical numerical data for conventional MBE growth of Si, the maximum value of the residual gas pressure is $\approx 10^{-5}$ Torr [24], well behind the UHV conditions present in the chamber. Again, one can assume that the time required for the deposition of 1 mono- layer (ML) of residual contaminants is 10^5 times those necessary for the deposition of 1 ML of film from the molecular beams. Consequently, it can be demonstrated that very low deposition rates (*i.e.* 1 ML s^{-1}) should be employed in an UHV environment [24]. However, it should be noted that p_r increases during

deposition due to the increased heat load from the effusion cells and the substrate. In the event that this occurs, a titanium filament sublimation pumping can reduce the residual gas pressure down to the minimum values. The entire vacuum system is bake able up to 250 °C for extended periods of time, to minimize outgassing from the internal walls during the deposition process. After a complete bake out cycle, the system with all the components installed reaches ~ 2×10^{-10} Torr, using only the main ion pump. Moreover, both CO_2 and H_2O gas pressure is drastically reduced by cooling the cryopanels with liquid nitrogen. Cryogenic temperatures act as an entangled for impurities, so vacuum levels of the orders of 10^{-11} Torr can be obtained. The substrate older is located a few centimeters away from the openings of the effusion cells, along the centerline of the system. The temperature of the substrate can be set during the deposition (from room temperature up to about 1400 °C), at a suitable temperature depending on the epitaxial process. It can also be heated before deposition primarily for cleaning and\or surface reconstruction, and afterwards for various heat treatments. As shown in Fig. **2**, the chamber is provided with a spectral mass analyzer to detect the residual atoms or molecules and thus to monitor the environment under which the film is grown.

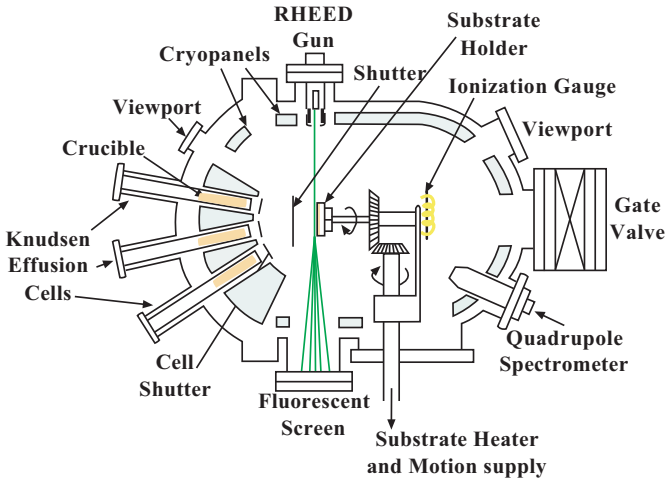

Figure 2: Schematic representation of a molecular beam epitaxy growth chamber. The main experimental features component the system are shown.

2.1. Effusion Cells

Fig. **2** shows three effusion cells, although as many as ten can be found in modern apparatus. A schematic illustration of a standard effusion cell is shown in Fig. **3 (a)**. In the growth of compound semiconductors the materials contained in the crucible could be the compounds themselves, their components, or different elements to be used as doping impurities. The crucible is usually made of pirolytic boron nitride (PBN), which can stand temperatures up to ~ 1400 °C without harmful material dissociation on the grown layers. Standard effusion cells are limited to operate at a temperature lower than 1200 °C, which is only just within the range of that required for Si, Ge, Al, Ga evaporation. The shape can be either cylindrical or conical, with different tapering angles, depending on the material to be evaporated as well as its diameter.

The total effusion rate can be approximately described by the Knudsen effusion equation [24]:

$$R = 8.33 \times 10^{22} \frac{p \cdot A_e}{\sqrt{M \cdot T}} \left[molecules\ s^{-1} \right] \quad \textbf{(1)}$$

where p is the pressure in the effusion cell, A_e is the surface area from which molecules evaporate, M is the molecular weight of the evaporating species and T is the temperature of the melt. Combining the Knudsen equation with the cosine law (given that the ideal Knudsen cell exhibits an angular distribution of the evaporated particles) [24], the impingement rate (also called flux) at the central point of the substrate axially aligned with the orifice can be written in the form:

$$I = 2.653 \times 10^{22} \frac{p \cdot A_e}{r^2 \sqrt{M \cdot T}} \left[mol\ m^{-2}\ s^{-1} \right] \quad \textbf{(2)}$$

where r is the distance between the orifice and impingement point. The rate at the edge point of the substrate, forming an angle θ with respect to central point can be easily calculated by multiplying the previous relation by $\cos 4\theta$. A standard effusive cell can assure flux stability greater than 1% during the deposition process, with a daily variation lower than 5% [25]. A Ta filament (or foils in other models) provides heating, while multiple Ta foils provide heat shielding to improve both the temperature stability and the thermal efficiency. Generally, a W-Re (5% and 26% Re) thermocouple is properly attached to both measure the material temperature and assure chemical stability. These refractory materials are thermally inert and suitable for operating at elevated temperatures.

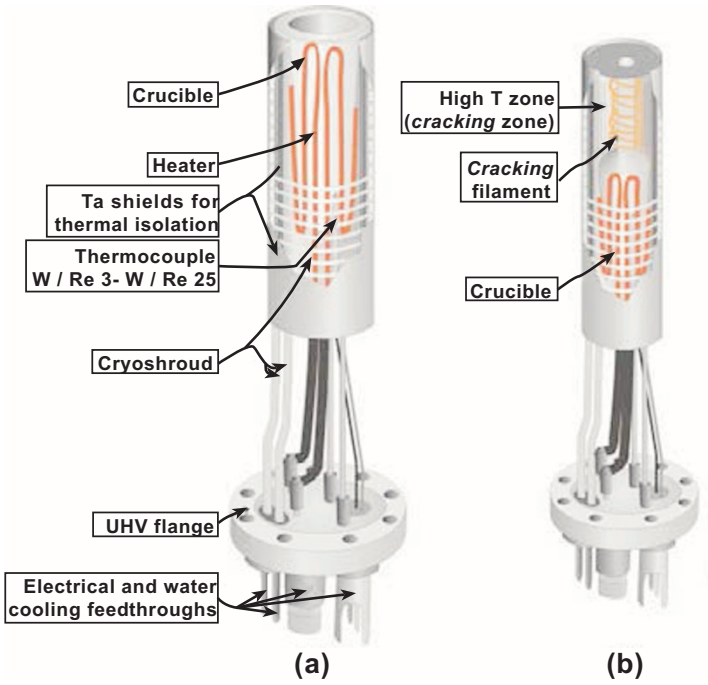

Figure 3: Schematic illustration of two present-day effusion cells used in MBE systems: (a) Standard Knudsen cell; (b) Two stage Cracking effusion cell (Courtesy of Prof. Klaus H. Ploog).

PID regulators provide high precision temperature regulation of ± 1 °C up to the maximum operating temperatures. Mechanical or pneumatic shutters, usually made of Ta or Mo, are placed in front of the orifices to trigger the fluxes (see Fig. **2**). The shutters operate faster than the growth rate (typically 0.1 s), and should be computer controlled to provide reproducible growth structures.

An important variation to the standard designs is provided by the so-called cracking cells. They are mainly employed for evaporation of group-V and VI elements (see Fig. **3 (b)**). In this cell, the material is first thermally evaporated (in form of tetramers) from the crucible; subsequently it passes through a hotter cracking zone where molecules are dimerized.

2.2. Electron Beam Evaporator

Molecular beams for MBE may also be generated by electron bombardment of suitable sources, by concentrating the heating energy onto just the evaporating load. The main property of this evaporation technique is the fast response process time, which permits high growth rates for low vapor pressure materials, especially when high purity of the evaporant is desired [26].

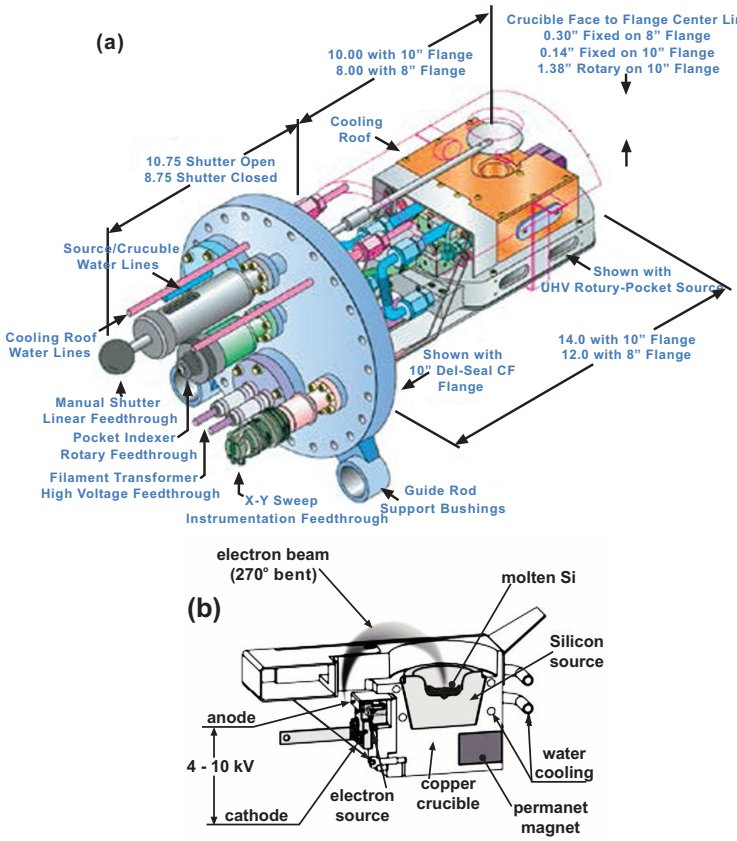

Figure 4: (a) Schematic overview of an electron-beam gun, with a horizontal source assembly (Courtesy of MDC Vacuum Limited). (b) Silicon electron bent-beam heated MBE source; electrons are forced into a curved path through a transverse magnetic field that permits focusing of the electron beam.

A proper filament emits electrons, and the stream is accelerated through a field of typically 4-10 kV. The electron gun is designed to eliminate nearly all ion bombardment effects on the filament thanks to the 270° electron beam deflection and the very sharply bent electron beam path near the exit of the aperture. Fig. **4 (a)** shows the inside of an electron gun mounted in a MBE chamber through 10" CF Flange. The figure shows the main assembly features including rotary, linear and electrical feedthroughs, clamps, linkages, water flow switch and water connections. In principle, due to the electrons impinging on the source, almost all the kinetic energy is converted into heat, and temperature exceeding 1500 °C may be obtained. During the film growth, the electron beam impinges on the center of the truncated cone of shaped source (Fig. **4 (b)**) [24]. For an electron beam current of 150 mA, the molten area can be lower than 10 mm in diameter. Electron beam evaporators are frequently used for evaporation of refractory metals, *e.g.* Mo, Nb, Ta, W, Zr, and are well suited for high-rate evaporation of Al, and of course for semiconductors like Si and Ge. Finally, a typical application is SiGe MBE for the generation of the main lattice element.

2.3. RHEED

For *in situ* monitoring of the thin films epitaxial growth, the system further incorporates a scanning high-energy electron diffraction apparatus, employing the small glancing angle reflection mode of operation (RHEED in Fig. **2**).

The feature of glancing incidence makes RHEED sensitive to the very uppermost layers, rather than the bulk structure. This tool reveals in real time changes either in the growing surface or in the surface structure (crystallographic orientation and morphology) of a thin film, without any interference with the growth process [27]. In RHEED, an incident electron beam strikes the sample's surface at near-grazing incidence (typically making an angle of incidence of lower than 3°) and is reflected onto a phosphorescent screen, as shown in Fig. **5**.

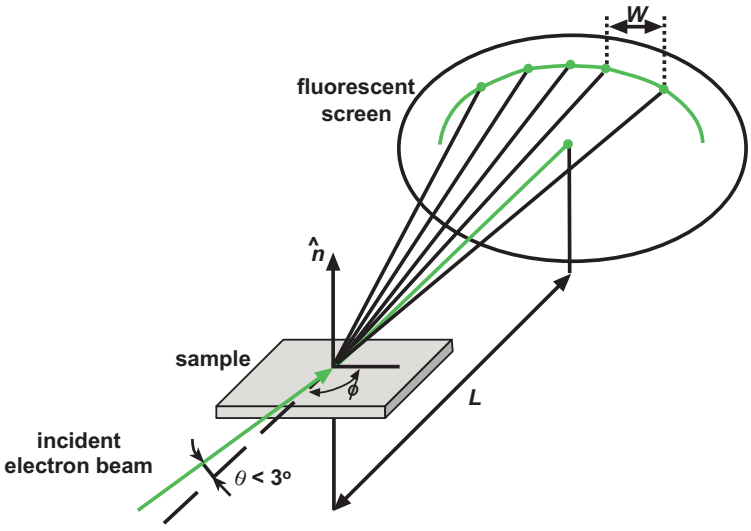

Figure 5: Schematic diagram of RHEED geometry showing the incident beam at an angle θ to the surface plane; ϕ is the azimuthal angle. W indicates the spacing among spot features; L is the distance between the point of incidence and the screen.

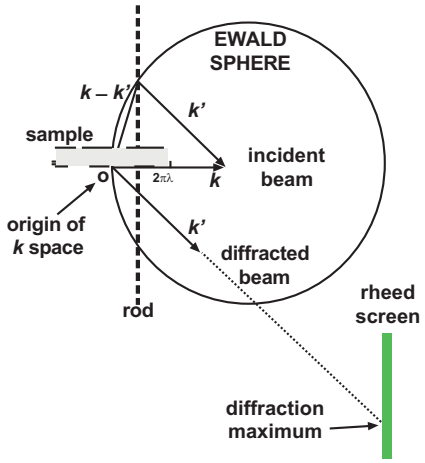

Figure 6: Intersection between the Ewald sphere and a particular reciprocal lattice rod. The corresponding electrons (having *k'* wave vectors) that satisfy this particular Laue condition form a diffraction spot on the screen.

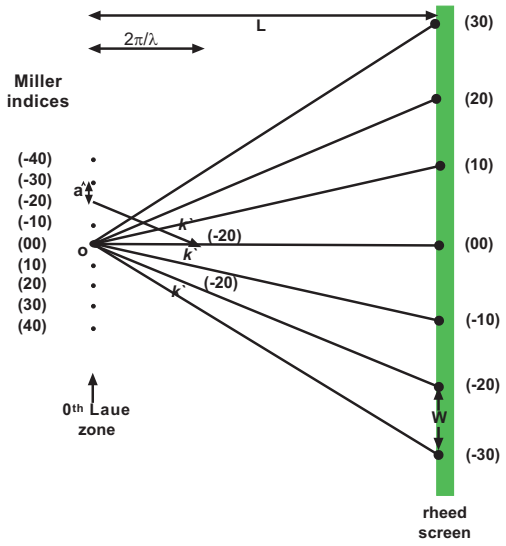

Figure 7: Schematic representation of the relation between the intrarow spacing a^* of the reciprocal lattice rods and the spacing W of the observed streaks.

In the framework of the Laue diffraction, the maximum intensity of the diffracted beams originates when the difference between the wave vectors of the incident and diffracted beams (*k* and *k'* respectively) intercept the reciprocal lattice rods. In this way it can be defined an Ewald sphere of radius *k* (Fig. **6**). The intersection of the Ewald sphere with the reciprocal lattice rods selects the electrons with wave vectors *k'*, forming some spots on the screen. If the surface is not flat, many electrons will be transmitted through surface asperities and scattered in different directions, resulting in a RHEED pattern constituted by many spotty features. However, thermal vibrations and lattice imperfections can cause the reciprocal lattice rods to have a finite thickness, while the

Ewald sphere itself has some finite thickness, due to divergence and dispersion of the electron beam [28].

Therefore, diffraction from a perfectly flat surface results in a diffraction pattern consisting of a series of streaks with modulated intensity (rather than points) superimposed on a fairly uniform background, due to inelastically scattered electrons. Therefore, RHEED analysis provides important information concerning the flatness of the growing film surface. Furthermore, it is evident that diffraction from an amorphous surface (such as an oxide on top of the substrate) gives no diffraction pattern at all. In this case only a diffuse background will result. The distance between the streaks of static RHEED pattern is an indication of the surface lattice unit cell size.

Fig. **7** shows a single row of rods that has a lateral spacing of a^* and indicate the Miller (hk) indices of several points of the reciprocal net; these same indices are given to their rods, and to the spots or streaks they create in the RHEED pattern. The observed streak spacing is W; the distance to the screen from the point of incidence is L. We may utilize the principle of similar triangles to show that $W/L \sim a^*/(2\pi/\lambda)$. Thus, the observed streak spacing indicates a rod spacing of:

$$a^* = \frac{2\pi \cdot W}{\lambda \cdot L} \tag{3}$$

where the wavelength $\lambda = 12.3/[V\,(1+1.95 \times 10^{-6}\,V)]^{1/2}$ Å, is expressed as function of the accelerating potential, V [28]. Potentialities of this method are expanded to oscillations of the electron beam reflected from a growing film surface in the process of MBE (RHEED oscillations) [29].

For a 2D growth, one oscillation period of a specular electron beam corresponds exactly to a monolayer of the film grown during this period. The oscillation period depends on the material flux to the surface, the substrate temperature and the growth mechanisms.

As an example, Fig. **8** compares different evolution of either RHEED intensity oscillation (left side) and RHEED patterns (right side) taken during and after, respectively, the growth of 5.5 ML (monolayers) of strained Ge on Si (100) at 400 °C, followed by heteroepitaxial Si growth at deposition rates with **(a)** and without **(b)** H supplies. The pattern **(c)** corresponds to case **(a)** followed, however, by a quick (1 min) after growth desorption annealing at 600 °C.

The top figures show the oscillation vanishing after 5 ML relative to the Ge cluster installation and the corresponding RHEED pattern signature. One oscillation period corresponds to the growth of one atomic ML [30].

3. SURFACE RECONSTRUCTION

A clean substrate is an important prerequisite for epitaxial growth, since its oxidation due to atmospheric exposure causes crystal defects that degrade both the optical and electrical features of the epitaxial layer. Nowadays, vendors supply ‘epi-ready’ wafers pre-cleaned and oxidized in a controlled environment, in order to form an oxide protective layer that can be removed inside the growth chamber.

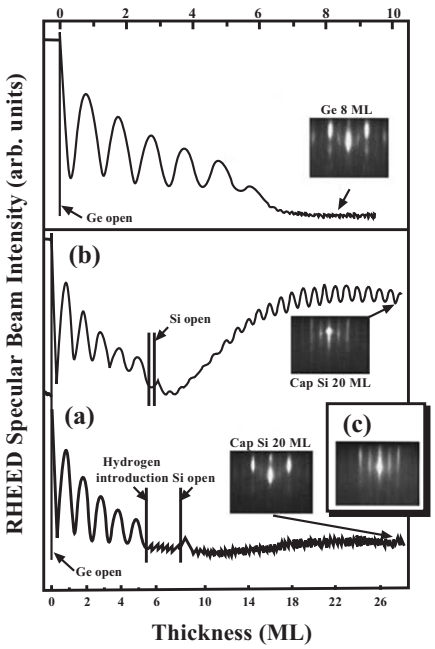

Figure 8: The top figure provides the corresponding signatures of an uninterrupted Ge growth. Si capping growth modes with (a) or without (b) hydrogen onto strained Ge. (c) Surface restoration and growth reorganization of the rough homogeneous Si covering into a smooth one (Elsevier license n. 2558160456690).

The use of such 'epi-ready' wafers has led to consistent results without the need for elaborate wafer cleaning procedures, such as Shiraki for the Si (100) and Si (111) [31], or Hakane for the Ge (100) [32]. However, even using 'epi-ready' substrates, proper thermal treatments must be used to obtain well-ordered surfaces after the oxide removal. In fact, in order to minimize the under coordinated surface, which presents one or more highly energetic dangling bonds, the system tries to arrange the surface atoms in different configurations, which differ from the bulk-like positions.

These new arrangements, involving the elimination of some atoms or their movement to non-epitaxial sites as well, are called surface reconstructions and deeply affect the further epitaxial processes.

The (001) is one of the most popular and widely studied surfaces for silicon and germanium.

It presents a very simple structure characterized, for the as-cut configuration, by square symmetry (see Fig. **9 (a)**, where the 1×1 surface unit cell is indicated). The surface lattice parameter is $a_s = a\sqrt{2}/2 = 3.84$ Å for Si and $a_s = 4.0$ Å for Ge, where a is the equilibrium bulk lattice constant. In the as cut geometry, each surface atom has two dangling bonds, making this a highly unstable configuration.

To reduce the dangling bonds density, neighboring Si atoms pair to form parallel dimmers, which represent the fundamental unit characteristic of the Si (001) (Fig. **9 (b)**). The dimerization has the

direct effect of modifying the surface periodicity along the direction of the dimer bond, leaving the perpendicular direction unchanged. Therefore, the reconstruction is defined as (2×1) Si (001). The dimerization process allows the system to reduce the number of unsatured bonds through the formation of a covalent directional σ bond connecting the two surface atoms. Moreover, the system can reduce its total energy by some hybridization processes, and reconstruction like $p(2\times1)$ and $c(4\times2)$ can be obtained (see Fig. **9 (c)** and **(d)** respectively).

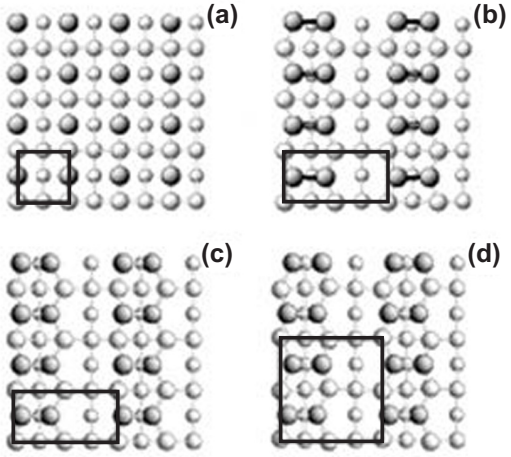

Figure 9: The topmost layer is painted in dark gray. (a) Top view of Si (001) in the as cut geometry, showing a surface unitary (1×1) cell. (b) (2×1) dimerized Si (001). (c) Dimerized Si (001) with all the dimers tilted along the same direction, forming a (2×1) periodicity. (d) Si (001) whose (2×2) dimers are tilted alternately along the dimmers row.

In the case of Si (111), the system presents the lowest dangling bond density over the surface area (d_H = 0.07 Å). Fig. **10 (a)** shows the top view of non-reconstructed Si (111).

Having such a low dangling bond density, the Si (111) is the cleavage surface obtained when an external strain is applied to split a Si crystal, but it is also one of the most frequently exposed surfaces when microcrystalline structures nucleate into amorphous matrix. The (111) surface assumes different reconstructions, like the π chain geometry (Fig. **10** (**b**)).

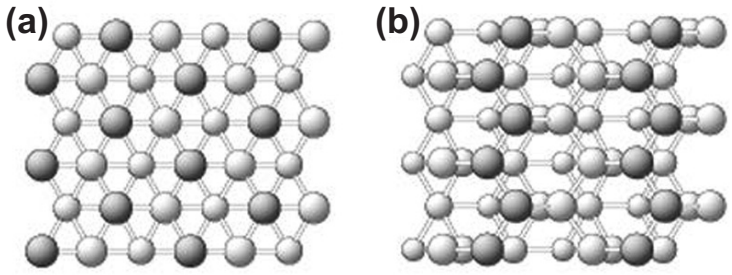

Figure 10: The topmost layer is painted in dark gray. (a) Top view of Si (111) in the as-cut geometry. (b) Top view of Si (111) π-chain.

4. DEPOSITION PROCESSES

The main substrate surface processes are schematically illustrated in Fig. **11**.

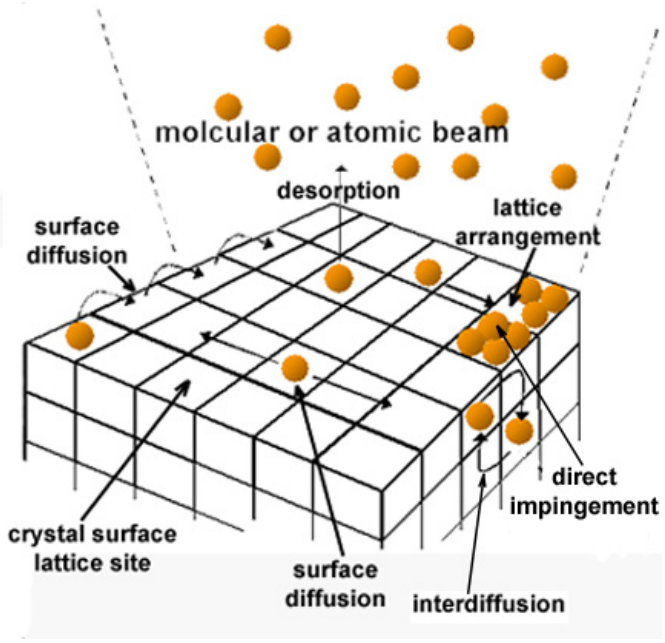

Figure 11: Schematic illustration of the surface processes occurring during MBE growth.

These processes involved during the epitaxial growth can be summarized as: a) adsorption of the evaporated atoms or molecules impinging on the surface; b) surface diffusion and dissociation of the absorbed atoms; c) atoms arrangement into the crystal lattice; d) thermal desorption of the species not arranged into the lattice [24]. The adsorbed molecules (or atoms) first combine to reach a critical size, **i**, and then become stable nuclei (or clusters) on the substrate. The main factors affecting **i** are the substrate temperature, the arrival rates and the affinity with the substrate. Subsequent molecules (or atoms) may condense directly onto these nuclei, decreasing the rate of formation of new nuclei and increasing the size of existing ones to form islands that may coalesce upon surface contact.

However, a distinction must be made in the initial growth process between the heteroepitaxial and homoepitaxial. Fig. **12** shows the behavior of the deposition rate as a function of arrival rate (the flux described by eq. 2), at a given substrate temperature. For the MBE growth of compound semiconductors, the required fluxes are typically between 10^{18}-10^{20} *atoms* m^{-2} s^{-1}.

Fig. **12 (a)** represents the case of a single component A. The dashed line indicates the asymptotic deposition rate applicable to both homoepitaxial growth at all stages and heteroepitaxial growth after nucleation. In order to initiate the nucleation process for heteroepitaxial growth at the given substrate temperature, the super saturation rate must be greater than the reevaporation rate: $R^S_A >$

R^E_A. The solid line indicates the case where other low-energy sites (*i.e.* surface impurities) are available to initiate the nucleation.

For a process involving an *AB* compound (see Fig. **12 (b)**) with a fixed evaporation rate of B, R_B, nucleation initiate when the evaporation rate of A exceeds the super saturation rate of the compound: $R_A > R^S_{AB}$. After nucleation, the deposition rate is proportional to R_A and becomes a constant, and R_B limits it. In the case of $R_A > R^S_A$ the deposition rate increases, and the growing film becomes A-rich [33].

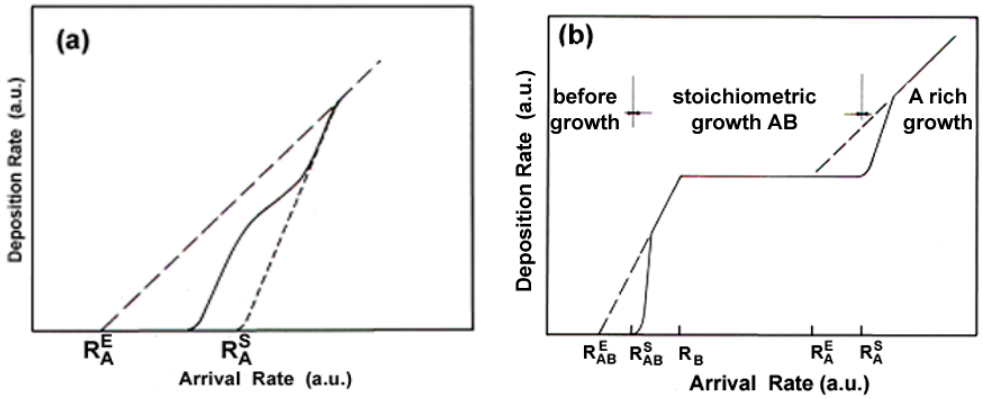

Figure 12: Schematic illustration of deposition rate *vs.* arrival rate of component A for (a) one component system; (b) two component system A and B, with a fixed arrival rate of component B. Superscripts E and S indicate reevaporation and super saturation, respectively.

The whole growth process can generally be described by few parameters, such as the sticking coefficient, s, the thermal accommodation coefficient, a_c, the condensation coefficient, c, the diffusion coefficient, D, and the mean stay time, τ_a:

$$s = \frac{N_{adh}}{N_{tot}} \quad \textbf{(4)}$$

the sticking coefficient is the ratio of the number of atoms (or molecules) adhering to the surface to the number of atoms (or molecules) arriving there. Depending on the growth regime, s could be less than unity when the adsorption energy of atoms is low, or the surface temperature is high;

$$a_c = \frac{T_i - T_e}{T_i - T_s} \quad \textbf{(5)}$$

the thermal accommodation coefficient defines the atoms (or molecules) fraction that is in thermodynamic equilibrium with the substrate. T_i is the effusion cell temperature; T_e is the energy corresponding temperature of atoms that immediately re-evaporate; T_s is the substrate temperature;

$$c = \frac{N'_{adh}}{N_{tot}} \tag{6}$$

the condensation coefficient, differently by *s*, describes the fraction of atoms (or molecules) that immediately adhere to the surface. In this case atoms (or molecules) are desorbed before their chemical-physical reaction to the surface;

$$D = \left(\frac{\alpha \cdot \upsilon}{N_0}\right) \exp\left(-\beta E_d\right)\left[cm^2\ s^{-1}\right] \tag{7}$$

the diffusion coefficient is defined as the product of the atom surface diffusion length before lattice incorporation and its surface mean speed. In this case α depends on the lattice parameter, υ is the atomic vibration frequency, N_0 (cm^{-2}) is the substrate sites number of equal adsorption energy E_a of isolated adatoms on the substrate, β is written for $(kT_s)^{-1}$, k is the Boltzmann's constant and T_s is the surface temperature;

$$\tau_a^{-1} = \upsilon \cdot \exp\left(-\beta E_a\right)\left[s^{-1}\right] \tag{8}$$

finally, τ_a is the atomic mean stay time on the substrate surface before their reevaporation [33, 24].

4.1. Processes of Nucleation and Growth

The formation of a large cluster is an example of a chain reaction that starts with the formation of a small stable nucleus. In fact, above the critical size (n > **i**), growth is more probable than decay, and all large clusters may be considered stable, even if some atoms leave them during the growth process. The single atoms can diffuse across the substrate to join a stable cluster, or they can impinge directly on the growing clusters and be incorporated by them, as illustrated in Fig. **11**. The binding energy E_j of a *j*-cluster (with size $j \geq$ **i**) can be related to the energy E_2 of a pair of atoms on the substrate, by considering nearest-neighbor bonds [34].

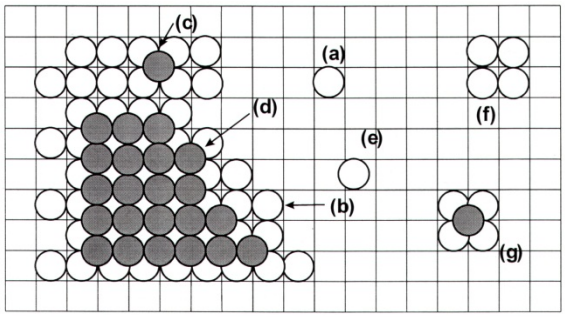

Figure 13: Binding energies of atoms and clusters that nucleate and growth on a square lattice. Single atoms: (a) E_a; (b) $E_a + 2E_2$; (c) $E'_a=4E_2$; (d) $E'_a+2E_2=6E_2$; (e) E_a-E_d; clusters; (f) $4E_a+4E_2$; (g) $4E_a+8E_2$. E_d is the diffusion energy; E'_a is the adsorption energy of an atom on a monolayer of the condensate; E'_d is the diffusion energy of an isolated atom on top of a monolayer; (f) and (g) refer to the 2D and 3D surface nucleation of clusters respectively.

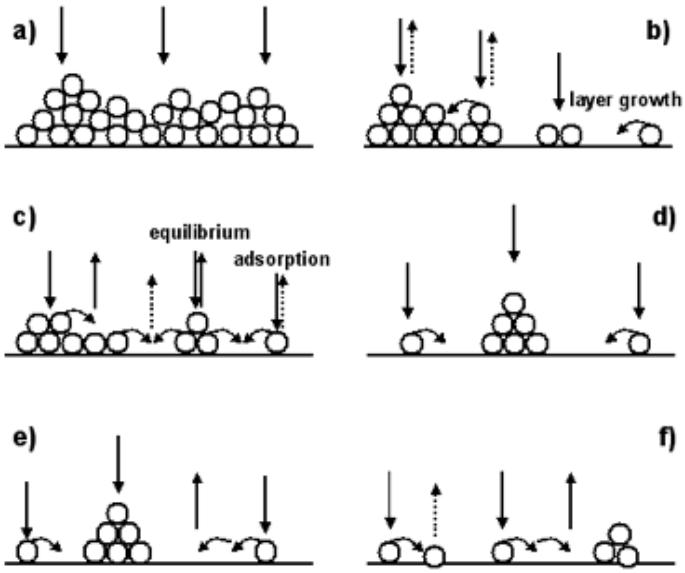

Figure 14: Regimes of nucleation and growth of clusters.

The processes are illustrated schematically in Fig. **13**, for an epitaxial growth in an orientation with four-fold symmetry. The three most important activation energies E_a, E_2 and E_d, with the experimental variables R and T_s, determine the nucleation regime observed (see Fig. **14**), which can be described using the parameter $R/N_0^2 D$. The growth process at the lowest temperature T_s and higher arrival rate R is described in Fig. **14 a)**. In this case $R/N_0^2 D \geq 1$ and the atoms stay exactly where they have arrived. An irregular layer is built up, and if atoms have directional bonds the layer will tend to be amorphous. The second regime, illustrated in Fig. **14 b)**, is the case of "layer-by-layer" growth. It is characterized by $R/N_0^2 D << 1$, $E_a \geq E'_a$, and T_s must be low enough so that 2D crystal layers can grow, even though single atoms may reevaporate. The regime illustrated in Fig. **14 c)** corresponds to the equilibrium adsorption, where the same conditions as case **b)** apply, but the surface temperature is higher or the arrival rate lower. Furthermore, atoms, at least from the highest layers, are quickly desorbed parallel to the surface, and the film growth only proceeds to a certain thickness whilst bulk crystals do not grow. In this case, there is no stable microstructure of the film in the long term, and adsorption is usually described only in thermodynamic terms.

In the regimes illustrated in Fig. **14 d)** and **e)** the film initially forms a three dimensional cluster on the substrate, the condition $4E_2 \geq E_a$ applies and the surface temperature is lower for case **d)** and higher for the case **e)**. If $E_2 > E_a$, the cluster will have a 3D shape from the beginning of growth. For the regime illustrated by case **d)**, all atoms condense, since the rate of formation of new clusters is faster compared to the rate of reevaporation, whilst for case **e)** the condensation is incomplete. Finally, in the regime illustrated in Fig. **14 f)**, if either E_2/kT or E_a/kT is small, the nucleation will be impossible on a perfect substrate, due to the effect of defects sites on the surface. An intermediate regime occurs when E'_a is lower than the value for an infinite crystal after some finite layers have been deposited. In this case growth starts in the "layer-by-layer" mode and then 3D crystals nucleate on the top. The term to describe this regime is the "Stranski-Krastanov"

growth mode [34]. The three growth modes previously described are schematically illustrated in Fig. **15**.

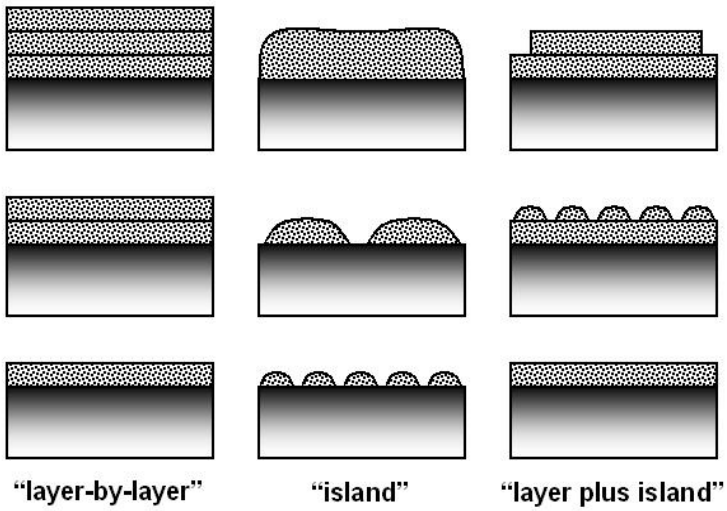

Figure 15: Schematic illustration of the three main growth modes: "layer-by-layer"-Frank-Van der Merwe; "island"-Volmer-Weber; "layer plus island"-Stranski-Krastanov.

These modes can also be classified by the behavior of the surface free energy during the epitaxial process, since it strongly determines the equilibrium morphology. In fact, considering a lattice-matched growth mode, in Frank-Van der Merwe, the sum of the free energy associated with the free surface of the epitaxial film, $\gamma_{e/v}$, and with the interface between the substrate and the epitaxial surface, $\gamma_{s/e}$, is less than or equal to that associated with the original substrate surface, $\gamma_{s/v}$. Then, the overall free energy decreases faster over the first layer (or two), before settling down to a steady state slope for thicker films. Therefore, the system is thermodynamically stabilized against breakup into inhomogeneous regions, some thicker and some thinner. In Volmer-Weber, the sum $\gamma_{e/v}$ and $\gamma_{s/e}$ is greater than $\gamma_{s/v}$. The overall free energy then increases over the first layer (or two), before reversing and decreasing as next layers are deposited. Therefore, the system of uniform thickness is thermodynamically unstable for breakup into inhomogeneous regions, some very thick and some completely uncovered. In Stranski-Krastanov, the sum $\gamma_{e/v}$ and $\gamma_{s/e}$ is less than $\gamma_{s/v}$. Therefore, the surface free energy decreases rapidly as the first layer (or two) is deposited, before decreasing, less steeply than the "layer-by-layer" growth mode, for thicker films. Therefore, films thicker than a few monolayers are unstable and can breakup into inhomogeneous regions, some very thick and some having only one layer (or two) [35]. For a strained epilayer there is the additional possibility that island formation may allow the system to introduce misfit dislocations underneath the islands to relax strain energy. For a system with small interface free energy but large lattice mismatch, initial growth is "layer-by-layer", but a thicker layer has greater strain energy and can lower its total energy by forming isolated thick islands in which the strain is relaxed by interfacial misfit dislocations [36].

5. MISFIT DISLOCATIONS AND DEFECTS

Generally, a heteroepitaxy process is related to lattice mismatch since a layer with atomic spacing or lattice symmetry different from those of the substrate is epitaxial grown. This disregistry can accommodate by strain connected to a relevant interfacial energy or by structural defects in the layer. In fact, when both the epilayer thickness and the mismatch between the stress-free lattice parameters of the two crystals are small, the separation of the dislocation becomes infinite and all mismatch is accommodated by elastic strain [37]. In order to introduce an easy explanation of the misfit concept, some important parameters will be considered, and the simplest situation where both layers have rectangular symmetry (i = x, y) at the interface plane is used. If the thickness of the epitaxial layer is thinner than that of the substrate, the mismatch parameter can be defined by:

$$f_i = \frac{a_{si} - a_{ei}}{a_{ei}} \tag{9}$$

where a is the lattice parameter and s and e indicate the substrate and the epitaxial layer, respectively. A positive value of f implies that the strain is tensile. Moreover, the misfit strain is defined as:

$$e_i = \frac{a^s_{ei} - a_{ei}}{a_{ei}} \tag{10}$$

where a^s_e indicates the lateral atomic spacing in the strained epilayer. However, when the coherence between the strained layer and the substrate is lost, the misfit strain is shared between a plastic strain component, d, due to the misfit dislocations and a residual elastic strain component:

$$f_i = e_i + d_i \tag{11}$$

The value of d can be estimated from the misfit dislocation spacing, S: $d = b_n/S$, where b_n is the interface-plane component of the Burgers vector in the direction of the misfit dislocation spacing. It is well known that under adequate conditions, overgrow layers can be deposited epitaxially on the substrate with different lattice parameters up to a critical thickness h_{crit} [38, 34]. Epilayers thinner than h_{crit} adapt the lattice parameter of the substrate, a condition known as "pseudomorphic" growth [39, 40].

The misfit between the substrate and the overgrown layer is sufficiently small, and the first deposited layers are strained to match the substrate and a coherent (perfect matched) epilayer is formed. The situation is depicted in Fig. **16**. If the lattice parameter of the epilayer is greater than that of the substrate, the film grown undergoes a compressive strain on the interface plane. *Vice versa*, the strain will be tensile. Moreover, since the total volume of the unit cell must remain unchanged, the cell is also distorted perpendicularly to the plane interface. As the epilayer thickness increases, overlapping h_{crit}, the homogeneous strain energy becomes favorable for the introduction of misfit dislocations (see Fig. **16**) [40]. Fig. **17** reports an example of the result of the Matthews-Blakeslee theory for 60° a/2 <101> misfit dislocation in the $Si_{1-x}Ge_x$/Si (100) system and experimental measurement of critical thickness h_{crit} for different growth\annealing temperatures [40]. It is also possible to change the value of h_{crit} by growing one or more

subsequent epilayers. In fact, if an epilayer B is deposited on a substrate A, and the layer thickness exceeds the critical value, it might be possible to restore coherency by the deposition of a layer of the same material of A.

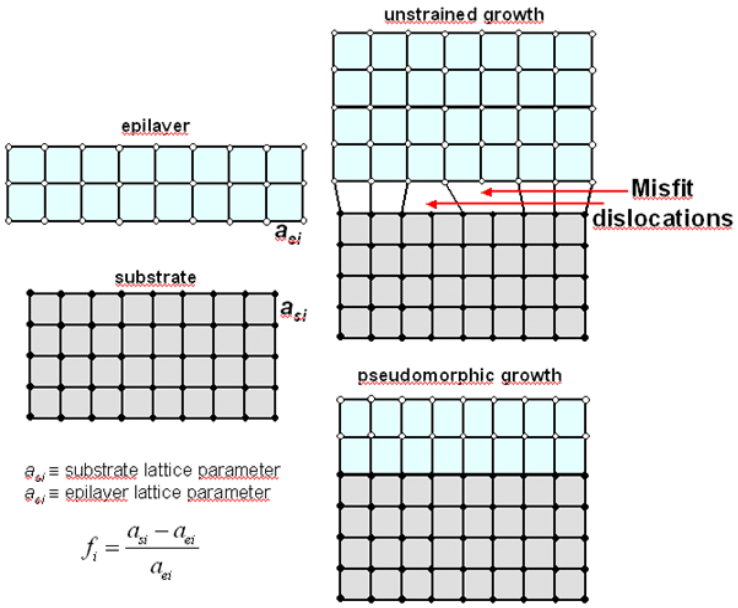

Figure 16: Growth of a layer on a substrate with different lattice parameters; the pseudomorphic (coherent mode) and the unstrained growth cases are illustrated. The red arrows indicate the presence of misfit dislocations at the interface, due to a non-coherent growth.

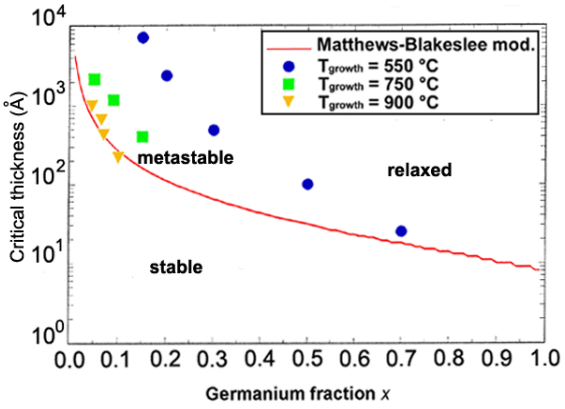

Figure 17: Measurement of critical thickness in the $Si_{1-x}Ge_x/Si$ (001) system for different growth temperatures *vs.* the prediction of the Matthews–Blakeslee model [40].

However, there is a second critical thickness of the epilayer B, above which it is not possible to restore coherency. Depending on the crystalline structure of the growing material and on the

quality of both the epitaxial process and the surface of deposition, a wide variety of dislocations and effects can originate in the epilayers. Even though the presence of most of these crystalline defects is undesirable, certain types are essential in semiconductor manufacturing. In the following sections the most common will be described briefly.

5.1. Dislocations

Considering a single epilayer in which the perfect coherent registry with the substrate is broken, the simplest consequence might consist of a half plane missing from the epitaxial film. In this case, the most useful definition to introduce is that related to the Burgers circuit. It is the atom-to-atom path that forms a closed loop in a crystal with dislocations. If the same atom-to-atom sequence is formed in a dislocation free crystal, and the circuit does not close, then the original loop must enclose one or more dislocations. The vector required to fill the gap in the circuit is called the Burgers vector (the red arrows illustrated in Fig. **18**).

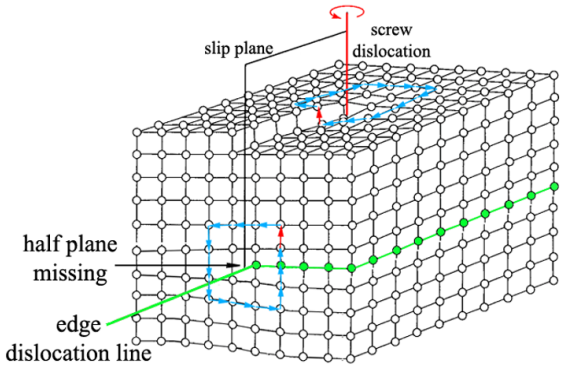

Figure 18: Pure edge and pure screw dislocations arising from the missing half of the epitaxial plane. The blue arrows indicate the Burgers vectors circuit. The red arrows indicate the Burgers vector $\vec{b}$.

In particular an edge dislocation has $\vec{b}$ perpendicular to the dislocation line. It marks the edge of a missing (or extra) half-plane of atoms. On the other hand, in a screw dislocation atoms are connected in a spiral around the screw dislocation. It has $\vec{b}$ parallel to the dislocation line. Generally, in most cases, the dislocation line lies at an arbitrary angle to its Burgers vector and the dislocation line has a mixed edge and screw character [41].

5.2. Stacking Faults

A stacking fault is a planar defect due to the interruption of the regular sequence layers within the crystal in a local region. This type of defect destroys the perfection of the host crystal, and the associated energy per unit area of fault is known as the “stacking fault energy”. Two types of stacking faults referred as to intrinsic and extrinsic are expected in a face centered cubic lattice. These are best described by considering the change in sequence resulting from the removal or introduction of an extra layer (see Fig. **19**).

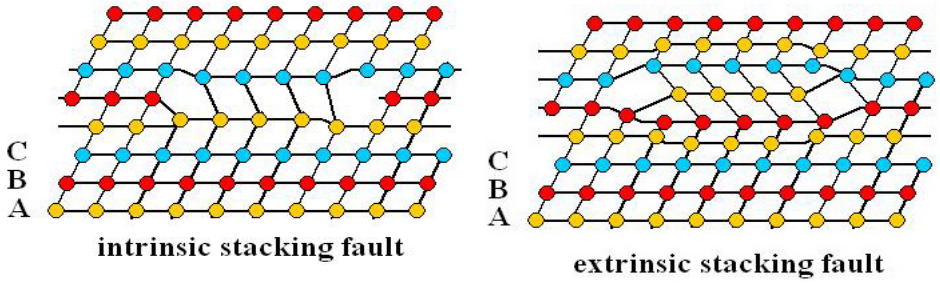

Figure 19: Stacking faults in the face-centered cubic structure.

In the intrinsic stacking fault, part of a layer has been removed which results in a break in the stacking sequence. Clearly, the stacking sequence above and below the fault plane are continuous right up to the fault itself. In the extrinsic stacking fault, an extra layer has been introduced. There are two breaks in the stacking sequence, and the extra layer does not belong to the continuing patterns of the lattice either below and or above the fault.

5.3. Grain Boundaries

A crystalline solid can also consist of a large number of randomly oriented grains (single crystals) separated by grains boundaries (defects). When the misorientation between the grains is too great, the atomic arrangements at the boundaries are very complex and vary significantly with the angles of misorientation (see Fig. **20**).

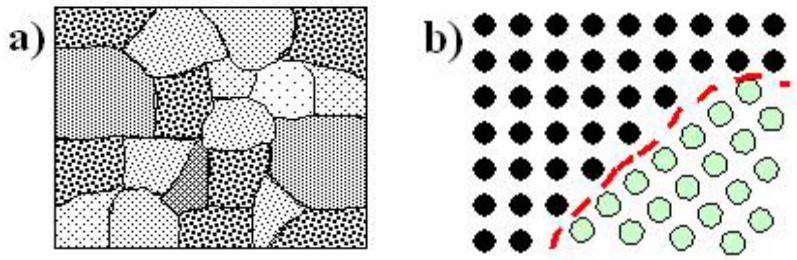

Figure 20: (a) Schematic illustration of differently oriented crystal grains in a polycrystalline material. (b) Representation of a grain boundary separating two crystallites.

A notable feature of the boundary structure is that the region of disorder is very narrow, limited to one or two atoms on each side of the boundary.

5.4. Twinning

Formation of twin boundaries is a process in which a region of a crystal undergoes a homogeneous shear that produces the original crystal structure in a new orientation. Deformation twinning can be induced by plastic deformation and is particularly important in body-centered and close packed hexagonal crystals. For example, in a face-centered cubic crystal the “ABC” notation adopted in

section **5.2** can be used to represent the relative atom positions in matrix and twin. Fig. **21** shows the stacking sequence of a (111) twin. The planes I-II and III-IV indicate the "coherent" twin planes; nearest-neighbor atom distances are unchanged across these planes. The plane II-III is called an "incoherent" twin plane; the two lattices do not fit exactly on them, and consequently there is considerable atomic misfit.

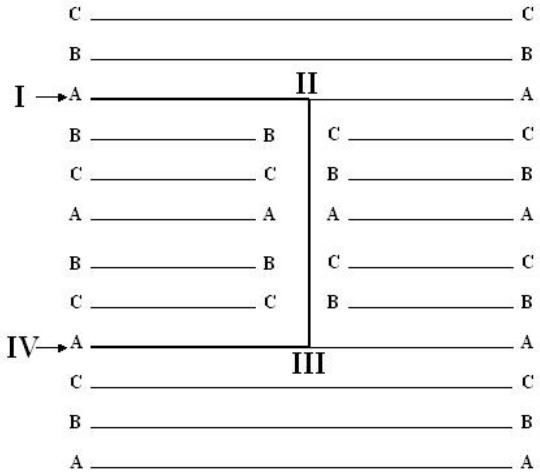

Figure 21: Stacking of (111) planes in a face-centred cubic crystal showing an embedded twin.

5.5. Point Defects

The 1D defect is called a point defect, since it involves only one atom surrounded by a perfect lattice. However, the presence of a point defect may affect the properties of its nearest neighbors, and by elastic interactions, a sizable spherical region of the lattice surround itself. Fig. **22** shows some forms of crystal point defects. A defect where an atom is missing from a lattice site is known as a vacancy defect. Vacancies are expected at high growth temperatures because the surface atoms mobility (*i.e.* the diffusion coefficient in eq. 7) in these cases must be quite high for them to change their positions leaving behind empty lattice sites.

If an atom is located in a non-lattice site within the crystal, it is said to be an interstitial defect. When the interstitial defect involves an extra atom, it is referred to as a self-interstitial defect. Vacancies and self-interstitial defects are classified as intrinsic point defects. A substitutional defect refers to an atom of a different type than the lattice composition, which has replaced one of the bulk atoms in the lattice. Substitutional and interstitial defects are classified as extrinsic point defects because foreign atoms are involved. If an atom leaves its site in the lattice, creating a vacancy, and then moves toward the surface of the crystal, it becomes a Schottky defect. On the other hand, an atom that vacates its position and transfers to an interstitial position in the crystal is known as a Frenkel defect. However, the management of defects during the epitaxial growth is an indispensable factor for obtaining materials with engineered performances (both electrical and optoelectronic). In fact, defects can be classified as undesired or desired impurities: the former generally refer to the contaminants into the lattice, the latter to the dopants.

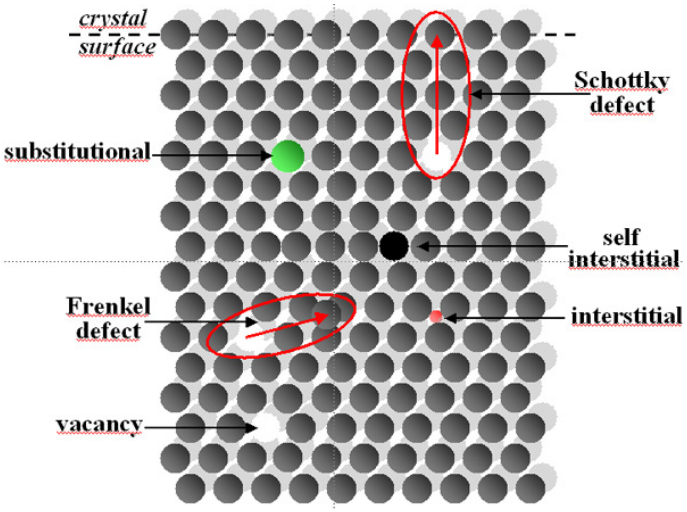

Figure 22: Schematic representation of the most common point defects in crystals.

6. DOPING

The main problem with the application of MBE for the fabrication of semiconductor devices is dopant incorporation. From a grower point of view, this topic should be divided into two parts: unintentional (and generally undesired) doping, which is caused by the presence of residual gases in the deposition chamber, and intentional (desired) doping, achieved for example by a thermal beam co-deposition process. As to the contribution of residual gas species, it should be noted that the value of the residual gas pressure achieved during the epitaxial deposition is lower than 5×10^{-11} Torr. At this low pressure the residual gas contains mainly H_2, H_2O, N_2 and CO_x molecules. In order to reduce to a minimum the incorporation of these contaminants it is a good practice turn off all hot filaments (such as the ionization gauges in Fig. **2**) not necessary during the epitaxial process. Moreover, it is important to restrict temporal and spatial variations in the temperature of LN_2 cryopanel surfaces during growth, as these spatial and temporal variations can result in variations in desorption and adsorption of trapped gas molecules. During the intentional doping of a semiconducting compound A^iB^j (A and B are the elements, while i and j are the numbers denoting columns in the Mendeleeev's table), different chemical reactions can take place [24]. If a cation element (A) is replaced by an element atom (C) of the group (i-1), a p-type doping is achieved:

$$C_g^{(i-1)} + V_{Ai} \leftrightarrow C_{Ai}^{(i-1)(-)} + h \qquad \textbf{(12)}$$

where V_{Ai} is a vacant A site in the A^iB^j compound, $C_{Ai}^{(i-1)(-)}$ is the ionized C acceptor, h is a free hole in the valence band of A^iB^j, and (g) denotes the gas phase of the element. If an anion atom (B) is replaced by an element atom (D) of the group (j + 1), an n-type doping is achieved:

$$\frac{1}{2} D_{2(g)}^{(j+1)} + V_{Bj} \leftrightarrow D_{Bj}^{(j-1)(+)} + e \qquad \textbf{(13)}$$

where e is a free electron in the conduction band of A^iB^j, $D_{Bj}^{(j-1)(+)}$ is an ionised donor. Replacement of a cation atom by doping atom (D) of the group $(i+j)/2$ of the periodic table gives n-type doping:

$$D_{(g)}^{(i+j)/2} + V_{Ai} \leftrightarrow D_{Ai}^{(i+j)/2(+)} + \left(j - i/2\right)e \tag{14}$$

Replacement of the anion atoms by doping elements (C) of the group $(i+j)/2$ gives p-type doping:

$$C_{(g)}^{(i+j)/2} + V_{Bj} \leftrightarrow C_{Bj}^{(i+j)/2(-)} + \left(j - i/2\right)h \tag{15}$$

However, the analysis of the previously illustrated reactions requires knowledge of quantities such as the enthalpy and entropy of the system of defects involved in the doping. A good approach to understanding the principles of this problem is that proposed by Heckingbottom [42], where thermodynamic considerations can determine whether a doping process is possible or not during the epitaxial deposition. This model is useful in the selection of dopants that are more suitable. In a more detailed study of a particular reaction, the comparison of the thermodynamic framework with experimental data provides identification of any kinetic barriers and hence leads to a clearer understanding of the reaction mechanism [43].

7. IV-GROUP MBE

The "Stranski-Krastanov" growth mode illustrated in sec. **4.1** is a powerful technique applied for fabrication of a large number of high-quality nanosized atomic clusters (quantum dots-QDs). These dots have unique properties which can be tuned by the grower by varying the epitaxial growth parameters. Due to the importance of Si in opto-electronic device applications and energetic device productions, nano-sized materials based on silicides are under continuous investigation to optimize their performance and to scale down dimensions. Arrays of Ge, Si and SiGe nano-islands, so called "pyramid" and "dome" clusters, grown on Si(001) are typical examples of such systems (see Fig. **23**). However, as previously illustrated, different growth conditions play crucial roles for the appearance of these islands grown on Si (001).

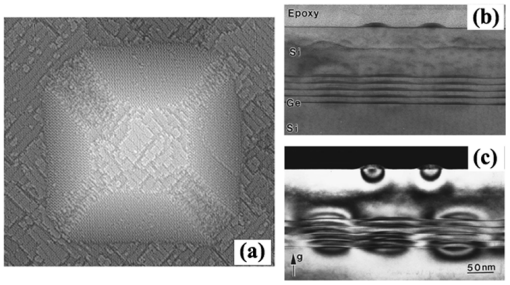

Figure 23: (a) Scanning Tunneling Microscopy (STM) image (108 × 108 nm^2) of a faceted island obtained by depositioning $Si_{0.6}Ge_{0.4}$ on Si (001) [44]. (b) Cross-sectional TEM image of a Ge/Si multilayer structure consisting of five individual Ge layers. (c) Dark field image exhibiting Ge islands buried in the Si layers (AIP license n. 2571411082174) [45].

Table **1** shows the results obtained by A. Malachias *et al.* [46], demonstrating how strong changes in interdiffusion and resulting atomic ordering arise from the different growth parameters used during the MBE deposition of Ge domes on Si(001). Another intriguing possibility is related to the formation of a patterned substrate, above which nanocrystals are subsequently self-assembled by solid phase epitaxy [47-49].

Table 1: Growth parameters used during MBE deposition of Ge:Si(001) films. Domes with different width/height ratio can be obtained.

Growth Temperature (°C)	Coverage	Dome width/height (nm)
620	6.7 ML Ge	87/19
700	11 ML Ge	143/36
750	11 ML Ge	170/34
840	6 ML Ge	338/37

Legend. The monolayer (ML) thickness is considered as 0.1413 nm for Ge, and 0.1385 nm for $Si_{0.5}Ge_{0.5}$.

In this model highly dense two-dimensional periodic arrays of ordered QDs can be nucleated, with lateral dimensions depending on the holes' properties. The 2D array of holes with different size, depth and pitches can be fabricated by a focused ion beam (FIB), both on SiO_2/Si(001) and Si(001) substrates. After the MBE evaporation of few monolayers of Ge (at room temperature), the system is annealed at about 500-550 °C, in order to raise the surface mobility of the Ge atoms, and then fill the holes by Ge QDs (see Fig. **24**). However, several theoretical models include the utilization of intermediate band solar cells [50], up-conversion for the absorption of sub-band gap light [51], and control of the strain, shape, and local Ge fraction in multicrystalline SiGe for the absorption of the near-infrared light [52]. Furthermore, experiments were also performed to improve the performance of the solar cells by 1) absorbing the low-energy photons, 2) by using SiGe multicrystalline with microscopic compositional distribution to enhance the absorption performance [53, 54], and 3) by exploiting the advantage of quantum well solar cells to independently optimise the absorption edge and spectral characteristics [55]. Another way to absorb the low-energy photon might be the incorporation of doped Ge dots in the intrinsic region of Si-based solar cells [23, 56-61].

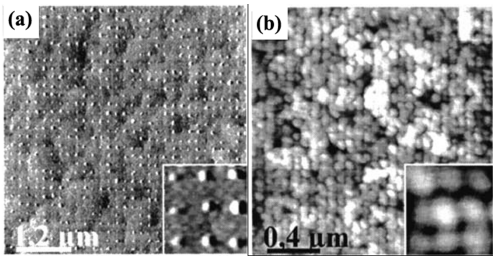

Figure 24: Atomic force microscopy (AFM) image of the organization of Ge dots on patterned areas by Ga^+ source (FIB), at a growth temperature of 550 °C and Ge thickness of 14. The initial holes diameter was 40 nm with a pitch of (a) 200 nm, and (b) 75 nm (AIP license n. 2573690146603).

Even though the MBE cannot represent a valuable growth technology for large production of semiconducting devices, it does represent an excellent way to investigate the basic properties of the materials and solutions previously mentioned, in order to employ them in either opto-electronic or energetic device applications produced by other industrial growth technologies widely used in the field of device fabrication.

ACKNOWLEDGEMENT

Declared none.

CONFLICT OF INTEREST

The author(s) confirm that this chapter content has no conflict of interest.

REFERENCES

[1] Cho AY. Film Deposition by Molecular-Beam Techniques. J Vac Sci Technol 1971; 8: S31-S38.
[2] Cho AY, Dunn CN, Kuvas RL, Schroeder WE. GaAs IMPATT diodes prepared by molecular beam epitaxy. Appl Phys Lett 1974; 25: 224-226.
[3] Cho AY, Ballamy WC. GaAs planar technology by molecular beam epitaxy (MBE). J Appl Phys 1975; 46: 783-785.
[4] Cho AY, Reinhart FK. Growth of three-dimensional dielectric waveguides for integrated optics by molecular-beam-epitaxy method. Appl Phys Lett 1972; 21: 355-356.
[5] Cho AY, Chen YS. Epitaxial growth and optical evaluation of gallium phosphide and gallium arsenide thin films on calcium fluoride substrate. Solid State Commun 1970; 8: 377-379.
[6] Cho AY. Epitaxial Growth of Gallium Phosphide on Cleaved and Polished (111) Calcium Fluoride. J Appl Phys 1970; 41: 782-786.
[7] Cho AY. Growth of periodic structures by the molecular beam method. Appl Phys Lett 1971; 19: 467-468.
[8] Dingle R, Wiegmann W, Henry CH. Quantum states of confined carriers in very thin $Al_xGa_{1-x}As/GaAs/Al_xGa_{1-x}As$ heterostructures. Phys Rev Lett 1974; 33: 827-830.
[9] Wachter M, Thonke K, Sauer R, SchaftIer F, Herzog HJ, Kasper E. Photoluminescence of confined excitons in MBE-grown $Si_{1-x}Ge_x/Si(100)$ single quantum wells. Thin Solid Films 1992; 222: 10-14.
[10] For a good collection of papers, see Proceedings on the Second International Conference on Modulated Semiconductor Structures, Kyoto: Japan 1985.
[11] Petroff PM, DenBaars SP. MBE and MOCVD growth and properties of self-assembling quantum dot arrays in III-V semiconductor structures. Superlattices Microstruct 1994; 15: 15-30.
[12] Leonard D, Krishnamurthy M, Reaves CM, Denbars SP, Petroff PM. Direct formation of quantum-sized dots from uniform coherent islands of InGaAs on GaAs surfaces. Appl Phys Lett 1993; 63: 3203-3205.
[13] Shen XQ, Tanaka S, Iwai S, Aoyagi Y. The formation of GaN dots on $Al_xGa_{1-x}N$ surfaces using Si in gas-source molecular beam epitaxy. Appl Phys Lett 1998; 72: 344-346.
[14] Waters RG, Wagner DK, Hill DS, Tihanyi PL, Vollmer BJ. High-power conversion efficiency quantum well diode lasers. Appl Phys Lett 1987; 51: 1318-1319.
[15] Wang J, Smith B, Xie X, Wang X, Burnham GT. High-efficiency diode lasers at high output power. Appl Phys Lett 1999; 74: 1525-1527.
[16] Fafard S, Hinzer K, Raymond S, *et al.* Red-Emitting Semiconductor Quantum Dot Lasers. Science 1996; 274: 1350-1353.

[17] Jo M, Ishida K, Yasuhara N, Sugawara Y, Kawamoto K, Fukatsu S. A Si-based quantum-dot light-emitting diode. Appl Phys Lett 2005; 86: 103509-3.
[18] Choi KK. The Physics of Quantum Well Infrared Photodetectors. River Edge, NJ; World Scientific 1997.
[19] Pan D, Towe E, Kennerly S. Normal-incidence intersubband (In, Ga)As/GaAs quantum dot infrared photodetectors. Appl Phys Lett 1998; 73: 1937-1939.
[20] Luque A, Martí A, López N, *et al.* Experimental analysis of the quasi-Fermi level split in quantum dot intermediate-band solar cells. Appl Phys Lett 2005; 87: 083505-3.
[21] Bimberg D, Grundmann M, Ledenstov NN. Quantum Dot Heterostructures. London: Wiley 1999.
[22] Alonso-Álvarez D, Taboada AG, Risalda JM, *et al.* Carrier recombination effects in strain compensated quantum dot stacks embedded in solar cells. Appl Phys Lett 2008; 93: 123114-3.
[23] Konle J, Presting H, Kibbel H, Banhart F. Growth studies of Ge-islands for enhanced performance of thin film solar cells. Mater Sci Eng B 2002; 89: 160-165.
[24] Herman MA, Sitter H. Molecular Beam Epitaxy. Berlin: Springer-Verlag 1989.
[25] Foxon CT, Joice BA. Growth and Characterisation of Semiconductors. Hilger: RA Stradling and PC Klipstein 1990.
[26] Malik RJ. Electron beam source molecular beam epitaxy of III–V compounds. J Vac Sci Technol B 1987; 5: 722-724.
[27] Somorjai GA. Treatise on Solid State Chemistry. New York: Hannay NB-Plenum 1976.
[28] Mahan JE, Geib KM, Robinson GY, Long RG. A review of the geometrical fundamentals of reflection high-energy electron diffraction with application to silicon surfaces. J Vac Sci Technol A 1990; 8: 3692-3700.
[29] Neave JH, Joyce BA, Dobson PJ, Norton N. Dynamics of film growth of GaAs by MBE from Rheed observations. Appl Phys A 1983; 31: 1-8.
[30] Dentel D, Bischoff JL, Kubler L, Bolmont D. Role of hydrogen during Si capping of strained Ge or $Si_{1-x}Ge_x$ hut clusters. Thin Solid Films 1998; 336: 49-52.
[31] Ishizaka A, Shiraki Y. Low temperature surface cleaning of Silicon and its application to Silicon MBE. J Electrochem Soc 1986; 133: 666-671.
[32] Hakane T, Okumura H, Tanaka J, Matsumoto S. New Ge substrate cleaning method for $Si_{1-x-y}Ge_xC_y$ MOMBE growth. Thin Solid Films 1997; 294: 153-156.
[33] Matthews JW, Ludeke R. Epitaxial Growth part A. New York: Academic Press Inc 1975.
[34] Matthews JW. Epitaxial Growth part B. New York: Academic Press Inc 1975.
[35] Tsao JY. Materials Fundamentals of Molecular Beam epitaxy. San Diego: Academic Press Inc 1993.
[36] Shaw DW, Bean JC, Keramidas VG, Peercy PS. Epitaxial Heterostructures. Pennsylvania: MRS 1990
[37] Matthews JW. Defects associated with the accommodation of misfit between crystals. J Vac Sci Technol 1975; 12: 126-133.
[38] Frank FC, van der Merwe JH. One-Dimensional Dislocations. I. Static Theory; II. Misfitting Monolayers and Oriented Overgrowth. Proc R Soc 1949; 198: 205-225.
[39] Finch AI, Quarrel AG. Crystal structure and orientation in zinc-oxide films. Proc Phys Soc 1934; 46: 148-162.
[40] Kasper E. Properties of strained and relaxed Silicon Germanium. London: INSPEC 1995.
[41] Hull D, Bacon DJ. Introduction to dislocations. Oxford: Butterworth-Heinemann 2001.
[42] Chang LL, Ploog K. Molecular Beam Epitaxy and Heterostructures. NATO ASI Ser, Ser E 87, Dordrecht: Martinus Nijhoff 1985.
[43] Heckingbottom R, Todd CJ, Davies GJ. The Interplay of Thermodynamics and Kinetics in Molecular Beam Epitaxy (MBE) of Doped Gallium Arsenide. J Electrochem Soc 1980; 127: 444-450.
[44] Tersoff J, Spencer BJ, Rastelli A, von Kanel H. Barrierless Formation and Faceting of SiGe Islands on Si(001). Phys Rev Lett 2002; 89: 196104-4.
[45] Kienzle O, Ernst F, Ruhle M, Schmidt OG, Eberl K. Germanium "quantum dots" embedded in silicon: Quantitavive study of self-alignment and coarsening. Appl Phys Lett 1999; 74: 269-271.

[46] Malachias A, Stoffel M, Schmidbauer M, *et al.* Atomic ordering dependence on growth method in Ge:Si(001) islands: Influence of surface kinetic and thermodynamic interdiffusion mechanisms. Phys Rev B 2010; 82: 035307-9.

[47] Karmous A, Cuenat A, Ronda A, Berbezier I. Ge dot organization on Si substrates patterned by focused ion beam. Appl Phys Lett 2004; 85: 6401-6403.

[48] Berbezier I, Karmous A, Ronda A, *et al.* Two-dimensional arrays of ordered, highly dense and ultra small Ge nanocrystals on thin SiO_2 Layers. J Phys Conf Ser 2005; 10: 73-76.

[49] Szkutnik PD, Sgarlata A, Motta N, Placidi E, Berbezier I, Balzarotti A. Influence of patterning on the nucleation of Ge islands on Si and SiO_2 surfaces. Surf Sci 2007; 601: 2778-2782.

[50] Cuadra L, Marti A, Luque A. Type II broken band heterostructure quantum dot to obtain a material for the intermediate band solar cell. Physica E 2002; 14: 162-165.

[51] Trupke T, Green MA, Wurfel P. Improving solar cell efficiencies by up-conversion of sub-band-gap light. J Appl Phys 2002; 92: 4117-4122.

[52] Usami N, Ichitsubo T, Ujihara T, *et al.* Influence of the elastic strain on the band structure of ellipsoidal SiGe coherently embedded in the Si matrix. J Appl Phys 2003; 94: 916-920.

[53] Nakajima K, Usami N, Fujiwara K, *et al.* Growth and properties of SiGe multicrystals with microscopic compositional distribution for high-efficiency solar cells. Sol Energy Mater Sol Cells 2002; 73: 305-320.

[54] Nakajima K, Usami N, Fujiwara K, *et al.* Melt growth of multicrystalline SiGe with large compositional distribution for new solar cell applications. Sol Energy Mater Sol Cells 2002; 72: 93-100.

[55] Barnham KWJ, Duggan G. A new approach to high-efficiency multi-band-gap solar cells. J Appl Phys 1990; 67: 3490-3493.

[56] Alguno A, Usami N, Ujihara T, *et al.* Effects of spacer thickness on quantum efficiency of the solar cells with embedded Ge islands in the intrinsic layer. Appl Phys Lett 2004; 84: 2802-2804.

[57] Yakimov AI, Markov VA, Dvurechenskii AV, Pchelyakov OP. Coulomb staircase in a Si/Ge structure. Philos Mag B 1992; 65: 701-705.

[58] Morresi L, Ayoub JP, Pinto N, *et al.* Structural, magnetic and electronic transport properties of MnxGe1-x/Ge(001) films grown by MBE at 350°C. Surf Sci 2007; 601: 2632-2635.

[59] Morresi L, Ayoub JP, Pinto N, *et al.* Formation of Mn5Ge3 nanoclusters in highly diluted MnxGe1-x alloys. Mat Sci Semic Proc 2006; 9: 836-840.

[60] Pinto N, Morresi L, Ficcadenti M, *et al.* Magnetic and electronic transport percolation in epitaxial GeMn films. Phys Rev B 2005; 72: 165203-7.

[61] Morresi L, Pinto N, Ficcadenti M, *et al.* Magnetic and transport polaron percolation in diluted GeMn films. Mat Sci Eng B 2006; 126: 197-201.